

Evidence and Effect of Photogenerated Charge Transfer for Enhanced Photocatalysis in WO₃/TiO₂ Heterojunction Films: A Computational and Experimental Study

Carlos Sotelo-Vazquez, Raul Quesada-Cabrera,* Min Ling, David O. Scanlon, Andreas Kafizas, Pardeep Kumar Thakur, Tien-Lin Lee, Alaric Taylor, Graeme W. Watson, Robert G. Palgrave, James R. Durrant, Christopher S. Blackman, and Ivan P. Parkin*

Semiconductor heterojunctions are used in a wide range of applications including catalysis, sensors, and solar-to-chemical energy conversion devices. These materials can spatially separate photogenerated charge across the heterojunction boundary, inhibiting recombination processes and synergistically enhancing their performance beyond the individual components. In this work, the WO₃/TiO₂ heterojunction grown by chemical vapor deposition is investigated. This consists of a highly nanostructured WO₃ layer of vertically aligned nanorods that is then coated with a conformal layer of TiO₂. This heterojunction shows an unusual electron transfer process, where photogenerated electrons move from the WO₃ layer into TiO₂. State-of-the-art hybrid density functional theory and hard X-ray photoelectron spectroscopy are used to elucidate the electronic interaction at the WO₃/TiO₂ interface. Transient absorption spectroscopy shows that recombination is substantially reduced, extending both the lifetime and population of photogenerated charges into timescales relevant to most photocatalytic processes. This increases the photocatalytic efficiency of the material, which is among the highest ever reported for a thin film. In allying computational and experimental methods, this is believed to be an ideal strategy for determining the band alignment in metal oxide heterojunction systems.

This phenomenon has been used advantageously in photovoltaics technologies as well as in organic and dye-sensitized solar cells^[1] and more recently in the field of photocatalysis, in particular for water-splitting applications.^[2] In a heterojunction, the band structures of the two coupled semiconductors may align favorably so as to encourage migration of photogenerated electrons (e^-) and holes (h^+) in separate directions across the heterojunction boundary. This vectorial separation reduces electron-hole recombination, and when used in photocatalytic systems, can enhance their efficiency.^[3–5] A remarkable example is the ubiquitous commercial TiO₂ P25 (Evonik, formerly Degussa), which consists of a \approx 3:1 ratio of anatase ($E_{\text{bg}} = 3.20$ eV) and rutile ($E_{\text{bg}} = 3.00$ eV) and is considered the benchmark photocatalyst.^[6] This heterojunction material, as well as many other successful systems such as Cu₂O/TiO₂,^[7] WO₃/BiVO₄,^[8] or ZnO/BiVO₄,^[9] have shown a clear

enhancement in their photoresponse compared to that of their individual analogues.

The synergistic interaction between different semiconductor phases strongly depends on the synthesis method and the physical properties of the resulting materials (particle size

1. Introduction

Heterojunction materials may benefit from charge transfer processes by coupling two semiconductors with appropriate band structures in order to drive a particular functionality.

Dr. C. Sotelo-Vazquez, Dr. R. Quesada-Cabrera, Dr. M. Ling, Dr. D. O. Scanlon, Dr. A. Kafizas,^[†] Dr. R. G. Palgrave, Dr. C. S. Blackman, Prof. I. P. Parkin
Department of Chemistry
University College London
20 Gordon St., London WC1H 0AJ, UK
E-mail: r.quesada@ucl.ac.uk; i.p.parkin@ucl.ac.uk
Dr. D. O. Scanlon, Dr. P. K. Thakur, Dr. T.-L. Lee
Diamond Light Source Ltd.
Harwell Science and Innovation Campus
Didcot OX11 0DE, UK

Dr. A. Taylor
Department of Electronic & Electrical Engineering
University College London
Torrington Place, London WC1E 7JE, UK

Prof. G. W. Watson
School of Chemistry and CRANN Institute
Trinity College Dublin
Dublin 2, Dublin, Ireland
Prof. J. R. Durrant
Department of Chemistry
Imperial College London
Exhibition Road, London SW7 2AZ, UK

^[†]Present address: Department of Chemistry, Imperial College London, Exhibition Road, London, SW7 2AZ

and shape, film thickness, specific surface area, crystallinity, etc.).^[5] It is important to note that a particular charge transfer direction should not be *assumed* solely on the grounds of band alignment. In fact, structural defects at the interface of two dissimilar phases may hamper or even reverse the expected electron transfer between them.^[10] For P25, it has been generally accepted that rutile acts as an electron sink in the anatase–rutile system.^[11] It has been assumed that an increased population of positive holes (h^+) on the anatase side promotes the formation of hydroxyl radicals, which in turn participate in oxidation reactions at the catalyst surface and hence enhance the activity of the material. However, recent computational and experimental evidence^[3,4,11] has suggested an oppositely staggered band alignment, where electrons transfer from rutile to anatase. The traditional observation of rutile as an electron sink may then be explained by the presence of deep electron trap states at the heterojunction interface, which can reverse the direction of charge transfer.

Heterojunction WO_3/TiO_2 materials have been widely employed in photocatalysis, showing a clear enhancement of their photoresponse upon ultraviolet irradiation.^[12–14] In these systems, electron transfer from TiO_2 ($E_{\text{bg}} = 3.20$ eV) to WO_3 ($E_{\text{bg}} = 2.74$ eV) is often inferred from a color change in WO_3 from yellow to blue upon photoexcitation. The color change is due to the formation of blue polarons (W^{5+}) upon reduction of W^{6+} ions, as evidenced by X-ray photoelectron spectroscopy (XPS).^[15] This charge transfer has been widely reported^[12,14,16] and correlates with the band alignment represented in **Figure 1A**. However, as we demonstrate in this work, it is possible to engineer a WO_3/TiO_2 system where electrons transfer from WO_3 to TiO_2 , according to the band alignment illustrated in **Figure 1B**. Herein, we have developed a nanostructured WO_3/TiO_2 film using chemical vapor deposition

methods, consisting of WO_3 nanorods of monoclinic structure, highly oriented in the [002] plane, coated with a thin conformal layer of anatase TiO_2 . Contrary to widely reported observation, our WO_3/TiO_2 heterojunctions preserved their original color and did not show any evidence of reduced tungsten species upon photoexcitation. Remarkably, our WO_3/TiO_2 heterojunctions showed record-high photocatalytic activity in the degradation of a model organic pollutant. State-of-the-art hybrid density functional theory (DFT), hard X-ray photoelectron spectroscopy (HAXPES), and transient absorption spectroscopy (TAS) were combined to investigate the band alignment of our WO_3/TiO_2 heterojunction and explain its outstanding photocatalytic activity. By allying such computational and experimental methods, we consider our approach a general strategy for determining the band alignment in metal oxide heterojunction systems.

2. Results

2.1. Synthesis and Physical Characterization

A range of heterojunction WO_3/TiO_2 thin films were deposited via a two-step process using chemical vapor deposition (CVD) methods. A high surface area WO_3 host, which consisted of WO_3 nanorods grown on a quartz substrate, was grown using aerosol-assisted CVD.^[17] XPS analysis showed that the WO_3 nanorods synthesized herein are substoichiometric and should be considered as WO_{3-x} , where $x = 0.026$; XPS results are discussed in depth below. Subsequently, these WO_3 nanorods were coated with a conformal TiO_2 layer using atmospheric-pressure CVD.^[4] Details of this synthesis procedure are given in the Experimental Section and the Supporting Information.

A schematic figure of the TiO_2 coating and corresponding cross-sectional scanning electron microscopy (SEM) images are shown in **Figure 2A**. The SEM studies confirmed that the microstructure of the WO_3 host was preserved after coating with TiO_2 . The average length of the WO_3 rods was estimated as ≈ 650 nm, which was found to be ideal from an optical point of view, as discussed below. High-resolution transmission electron microscopy (HRTEM) analysis showed that the WO_3 nanorods were completely encapsulated within the TiO_2 overlayer (**Figure 2B**), forming a core–shell type structure. Complementary energy-dispersive X-ray spectroscopy (EDS) analysis across the nanorods showed a maximum Ti concentration at both edges and the presence of W solely in the core, suggesting no significant W diffusion into the TiO_2 layer. These studies revealed the presence of W, Ti, and O only, with no additional impurity elements. EDS showed that the WO_3 nanorods were ≈ 60 nm in diameter and that the TiO_2 coating was ≈ 100 nm thick.

X-ray diffraction analysis of the WO_3/TiO_2 heterojunction and its individual analogues

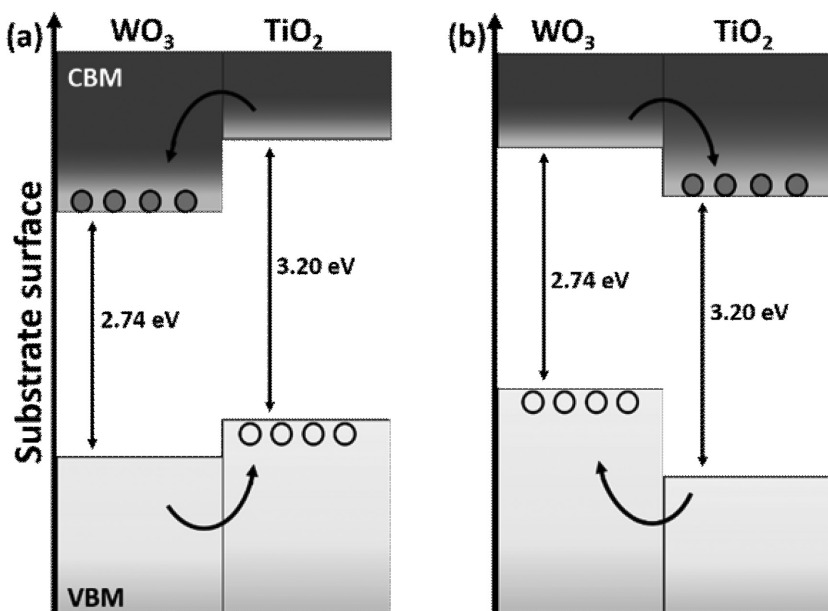


Figure 1. Schematic illustration of two possible band alignments in the WO_3/TiO_2 heterojunction system. Both models are of a staggered type II alignment. A) In the model, photogenerated electrons (full circles) transfer from TiO_2 to WO_3 and holes (empty circles) transfer from WO_3 to TiO_2 . B) In the proposed model for our materials, a reverse charge transfer is observed.

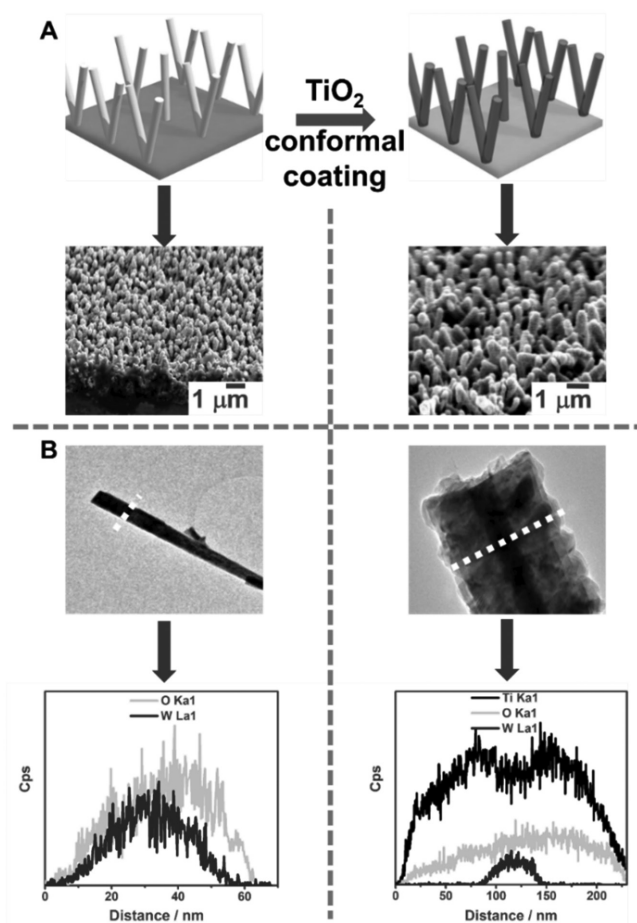


Figure 2. A) Schematic illustration of the coating of WO_3 nanorods with TiO_2 and their corresponding cross-sectional scanning electron microscopy (SEM) images. B) High-resolution transmission electron microscopy (HRTEM) images of individual WO_3 nanorods, before (left column) and after (right column) coating with TiO_2 and the corresponding energy dispersive X-ray spectroscopy (EDS) analysis performed across the dotted white line.

showed the formation of pure monoclinic WO_3 and anatase TiO_2 structures (Figure 3A) with no trace of additional phases or impurities. Le Bail refined models of the X-ray diffraction (XRD) patterns showed no substantial change in unit cell volume for either phase (Table 1), further indicating that no ion diffusion had occurred during the deposition of the TiO_2 overlayer. The corresponding average crystal sizes, determined from diffraction peak widths, did not change significantly from the individual analogues. Raman spectroscopy corroborated our XRD findings, showing the solitary presence of anatase TiO_2 and monoclinic WO_3 phases (Figure 3B). Of note, the position of the main Raman scattering band for anatase ($E_g \approx 144 \text{ cm}^{-1}$) is very sensitive to the incorporation of ions within the TiO_2 unit cell.^[18] In our WO_3/TiO_2 heterojunctions there was no shift in this band, which again showed that ion diffusion had not occurred.

2.2. Optical Properties

UV-vis spectroscopy was used to study the optical properties of the WO_3/TiO_2 film and its individual analogues (i.e., the WO_3

nanorods before the TiO_2 coating and a conventional TiO_2 film deposited on a plain glass substrate). From Figure 4A, it can be inferred that the single-component TiO_2 film showed the expected absorption edge of the anatase phase at $\approx 380 \text{ nm}$. By contrast, the plain WO_3 nanorods showed an absorption edge higher than expected for a WO_3 film, which can be explained in terms of the synthesis method employed. It has been recently found by Ling et al.^[19] that aerosol-assisted CVD can be used to deposit WO_3 nanorods containing oxygen vacancies, which induce a quantum confinement effect. The existence of oxygen vacancies was inferred from the presence of a small amount of reduced tungsten species ($\text{W}^{5+/4+}$) in the as-deposited WO_3 film,^[20] as observed by XPS analysis (Figure 4B) and the requirement for charge neutrality. Deconvolution of the W 4f region indicated a relative $\text{W}^{5+/4+}$ concentration of $\approx 2.60 \text{ at}\%$. The formation of dislocation loops within the WO_3 layer would widen the material bandgap, as shown by our Tauc plot analyses,^[21] revealing respective bandgaps of ≈ 3.2 and 3.05 eV for the TiO_2 and WO_3 single-component materials (Figure 4C). However, it is interesting to note that the spectrum of the WO_3/TiO_2 heterojunction was red-shifted to values more akin to bulk WO_3 materials (typically 2.8 eV), with an estimated bandgap of 2.85 eV .

2.3. Hybrid DFT and HAXPES Analyses

Further investigation from both theoretical and experimental standpoints was carried out in order to understand the electronic interaction at the WO_3/TiO_2 heterojunction. DFT has been widely used to ascertain the electronic band alignment between semiconductors.^[22,23] The ionization potential of bulk WO_3 was calculated using the slab model,^[24] using hybrid DFT (Heyd-Scuseria-Ernzerhof (HSE06) functional^[25]) within the Vienna Ab initio Simulation Package (VASP) code. In Figure 5, the alignment is plotted relative to the anatase TiO_2 band edges as calculated previously.^[3] The HSE06 calculated ionization potential (7.65 eV) and electron affinity (4.91 eV) for WO_3 fits reasonably well with previous experimental measurements of 7.38 ± 0.11 and $4.10 \pm 0.11 \text{ eV}$ for WO_3 surfaces.^[26] It should be noted that our calculated ionization potentials do not take into account the effects of interfacial strain and chemical interactions that may influence the band offset at a particular interface; however, they offer a reasonable first approximation, as demonstrated by the widespread application of Anderson's rule for estimating band offsets.^[27] Our calculated alignment suggests spatial separation of holes moving into WO_3 (Figure 5). This idealized alignment is at variance with the commonly accepted $\text{WO}_3\text{-TiO}_2$ alignment motif in the literature.^[12]

Further understanding of the electronic processes at the WO_3/TiO_2 interface was revealed from HAXPES measurements carried out at Beamline I09 at Diamond Light Source. Figure 6A shows the valence band spectra measured from the WO_3/TiO_2 heterojunction film and its individual components. It is worth mentioning that no differences in the binding energy of either Ti 2p or W 4d were detected between the coated nanorods and the corresponding references (see Figure S2A,B, Supporting Information), indicating that the contact between WO_3 and TiO_2 does not alter the energy levels relative to the vacuum level

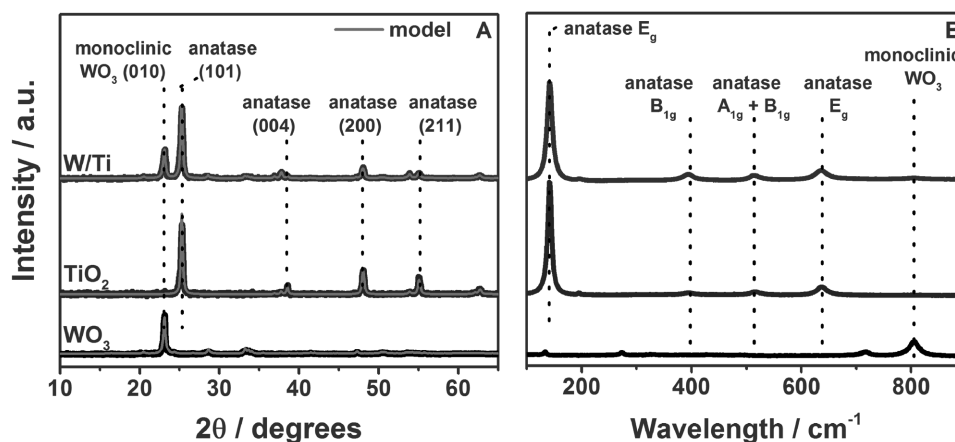


Figure 3. A) X-ray diffraction patterns of the WO_3/TiO_2 heterojunction film (W/Ti) and its analogues, WO_3 nanorods and anatase TiO_2 ($\lambda = 1.54 \text{ \AA}$). The data were fit to a Le Bail refined model (gray lines). B) Raman spectroscopy analysis showing the presence of pure anatase TiO_2 and monoclinic WO_3 phases. The corresponding XRD peaks and Raman modes of TiO_2 and WO_3 standards (dotted lines) are included for reference.

on either side of the interface. A small band observed at $\approx 0.5 \text{ eV}$ in the WO_3 layer is due to the presence of a small number of W^{5+} defects, typical of WO_3 .

The valence band alignment across the WO_3/TiO_2 interface could thus be determined directly from the valence band maxima of the WO_3 and TiO_2 references, which were extracted from Figure 6A to be 2.85 and 3.57 eV below the Fermi level, respectively, leading to a valence band offset of 0.72 eV. Figure 6B summarizes the alignment of the energy levels derived from the HAXPES data, where the conduction band offset was estimated to be 0.26 eV, using previously reported bandgaps of 2.74 and 3.2 eV for WO_3 and TiO_2 , respectively. It can be seen that the band edge of WO_3 is above that of TiO_2 for both conduction and valence bands, in excellent agreement with our DFT calculations.

2.4. Transient Absorption Spectroscopy

TAS is a form of laser flash spectroscopy that can monitor the generation, recombination, trapping, charge transfer, etc. of photogenerated charges in semiconductors.^[28–30] The dynamics specific to photogenerated electrons or holes can be studied by tracking transient changes in absorbance at particular

wavelengths.^[31] The technique has primarily been used to study charge transfer processes in solar cells (organic–organic or inorganic–organic),^[32,33] but has also been used to study charge transfers in heterojunction photocatalysts (inorganic–inorganic)^[34] as well as the kinetics of photocatalytic processes.^[35,36] In this article, our TAS measurements focused on long-lived charge carriers (micro- to millisecond) whose yields and lifetimes are critical to photocatalytic function.^[37] The study was carried out in diffuse reflectance mode, since the materials were highly light scattering. A comparison between the TAS measurements of our WO_3/TiO_2 heterojunction film and its individual analogues is shown in Figure 7A. It can be seen that 10 μs after the excitation pulse ($\lambda = 355 \text{ nm}$, 1.2 mJ cm^{-2}), the absorption increase was approximately four times greater than TiO_2 . It is worth noting that the pure TiO_2 sample investigated here was 200 nm thick and thus of similar thickness to the TiO_2 overlayer present in our WO_3/TiO_2 heterojunctions.

Chemical scavenger studies of both WO_3 and TiO_2 have shown that photogenerated hole carriers mostly absorb in the near-UV region ($\lambda_{\text{max}} \approx 450 \text{ nm}$) and electrons in the near-IR ($\lambda_{\text{max}} \approx 900 \text{ nm}$).^[10,29] These chemical scavengers are typically required in the case of WO_3 in order to observe charge carriers on the microsecond timescale.^[29] This explains the low signals found in WO_3 (Figure 7A), since the measurements

Table 1. Unit cell lattice parameters derived from Le Bail refinement of XRD data. (wRp is the weighed residual of least-squares refinement. V (%) is the lattice volume expansion relative to a powder standard. τ is the average crystallite size. Numbers in parentheses represent the error on the last digit.)

Sample	X-ray diffraction-Le Bail refinement					
		a [\AA]	c [\AA]	V [%]	wRp	τ [nm]
Standards	WO_3	7.301(1)	7.670(1)	–	–	–
	TiO_2	3.785(1)	9.512(1)	–	–	–
Pure phase	WO_3	7.287(3)	7.701(1)	0.02	0.12	27.3
Pure phase	TiO_2	3.785(1)	9.525(3)	0.13	0.16	32.6
WO_3/TiO_2	WO_3	7.301(6)	7.710(1)	0.49	0.12	23.2
	TiO_2	3.788(1)	9.515(2)	0.22	–	26.8

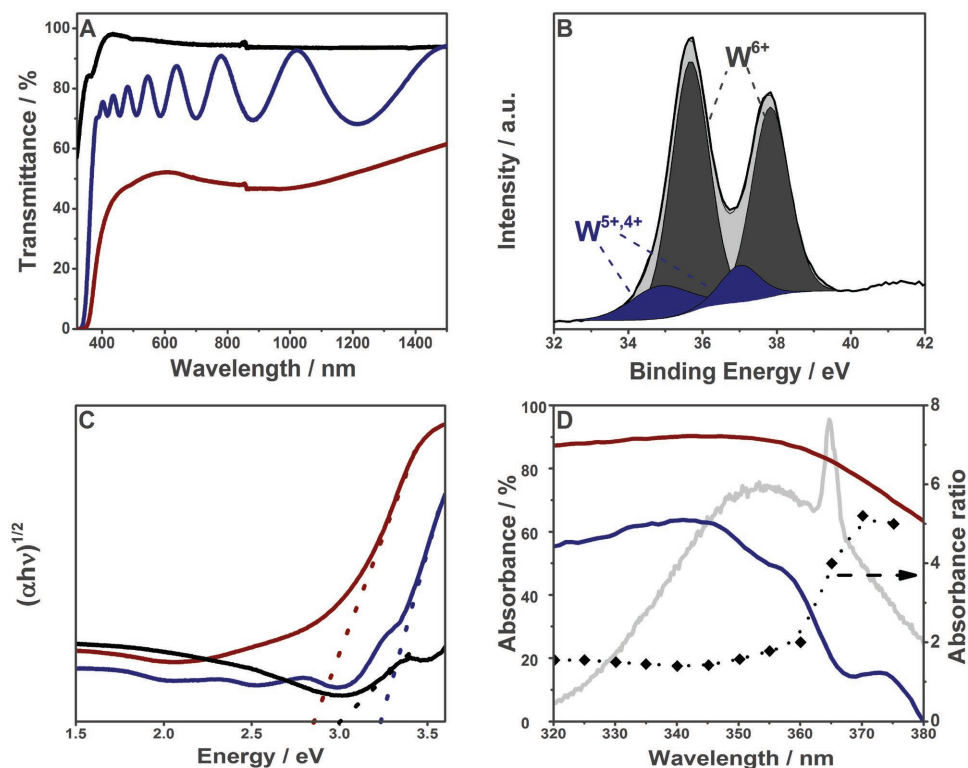


Figure 4. A) Transmittance spectra of WO₃ (black line), TiO₂ (blue line), and the WO₃/TiO₂ film (red line). B) X-ray photoelectron spectroscopy (XPS) spectrum of the W 4f environment in films of WO₃. The gray filling is assigned to W⁶⁺ states and the blue filling is assigned to W^{5+/4+} states. C) Corresponding bandgap energies derived from Tauc plot analyses. D) Absorption spectra of the TiO₂ (blue line) and the WO₃/TiO₂ (red line) films in the UV region. The emission spectrum of the UV light source (gray line) used in our photocatalytic tests is included for reference. The dotted line indicates the ratio between the absorbance of the two films.

were conducted in the absence of chemical scavengers. Transient absorption signals were lost as electrons and holes recombined. This occurred before the timescale of our measurements in WO₃, and substantially more slowly in TiO₂ and WO₃/TiO₂ heterojunction films. The kinetics of electron-hole recombination in our single-component TiO₂ was similar to previous

studies.^[37,38] If we focus on changes in the transient absorption at 950 nm, which corresponds to photogenerated electrons,^[10,29] the rate of recombination is significantly slower within the WO₃/TiO₂ heterojunction compared with TiO₂ (Figure 7B). Because of the strong overlap of charge carriers in WO₃ and TiO₂, our TAS studies could not reveal where the charges

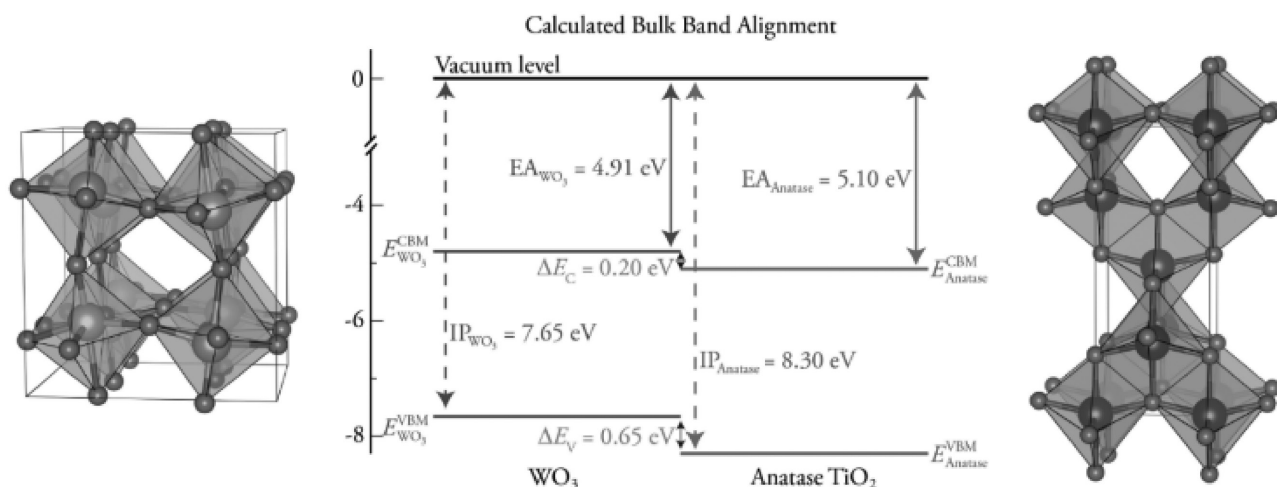


Figure 5. HSE06 calculated band alignment between monoclinic WO₃ and anatase TiO₂. The electron affinities are calculated based on bandgaps of 2.74 and 3.20 eV for WO₃ and TiO₂, respectively.

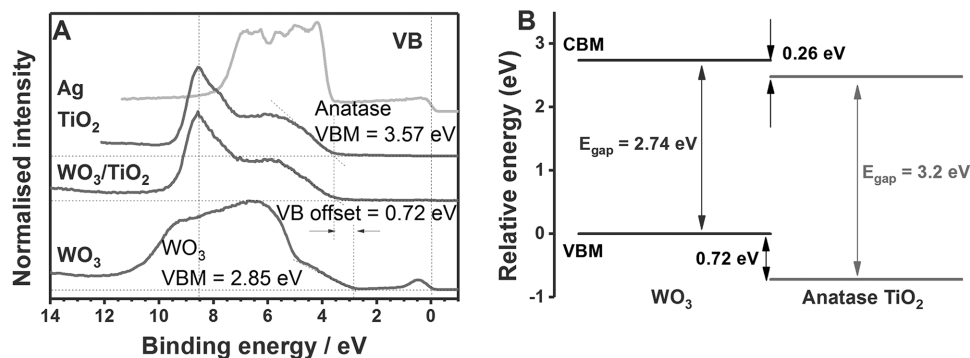


Figure 6. HAXPES measurements of the WO₃/TiO₂ heterojunction film and the individual components, monoclinic WO₃ and anatase TiO₂ films. A) Corresponding valence band spectra of the three materials. For each sample a silver Fermi edge was recorded to calibrate the binding energies. The blue dashed lines mark the valence band maxima of the TiO₂ and WO₃ references. B) Band alignment at the WO₃/TiO₂ interface derived from HAXPES results. The conduction band offset was estimated from bandgap energies reported in the literature. The values given are relative to the VBM of WO₃.

migrated in the heterojunction. However, our results do show that in forming a WO₃/TiO₂ heterojunction both the number of long-lived charge carriers and their lifetime are enhanced.

2.5. Photocatalytic Activity

The photocatalytic activities of the WO₃/TiO₂ film and their analogues were evaluated against the degradation of a model organic pollutant, octadecanoic (stearic) acid, under ultraviolet (UVA) illumination ($I = 3.15 \text{ mW cm}^{-2}$).^[39] Details of the photocatalytic test are given in the Experimental Section and the Supporting Information. The rates of degradation were conveniently expressed in terms of formal quantum efficiency (ξ , units, molecules photon⁻¹), defined as molecules of stearic acid degraded per incident photon. The corresponding values are listed in Table 2. The photocatalytic activity of the heterojunction film (17.1×10^{-4} molecules photon⁻¹) was clearly superior to those of the WO₃ and TiO₂ individual analogues (0.4×10^{-4} and 1.3×10^{-4} molecules photon⁻¹, respectively). If we consider the number of electron transfers required to completely photocatalyse stearic acid (104 electrons),^[40] then a formal quantum efficiency of 17.1×10^{-4} molecules photon⁻¹ corresponds

to a photocatalytic efficiency of $\approx 18\%$ per incident photon. Figure 8 compares these ξ values with those obtained using standard samples. Remarkably, the activity of the WO₃/TiO₂ thin film was comparable to that of a thick TiO₂ P25 Evonik film (16.8×10^{-4} molecules photon⁻¹) prepared following a method from the literature (see Supporting Information).^[41] As a reference, this study included a commercially available self-cleaning coating, Pilkington Activ glass obtained from Mills et al.^[42] (Figure 8), which showed a ξ value of 0.2×10^{-4} molecules photon⁻¹. It is worth noting that the activity of the WO₃/TiO₂ film exceeded that of a highly active heterojunction rutile/anatase TiO₂ film (10.7×10^{-4} molecules photon⁻¹) previously synthesized in our group (Table 2 and Figure 8).^[4] The ξ values were also highly reproducible, even after storage for one year (Figure S3, Supporting Information).

3. Discussion

Many research groups have investigated the interaction between WO₃ and TiO₂ using different synthesis methods.^[12–14,43–45] Commonly, these resulted in triclinic WO₃ as opposed to the monoclinic structure formed in this work, which also showed

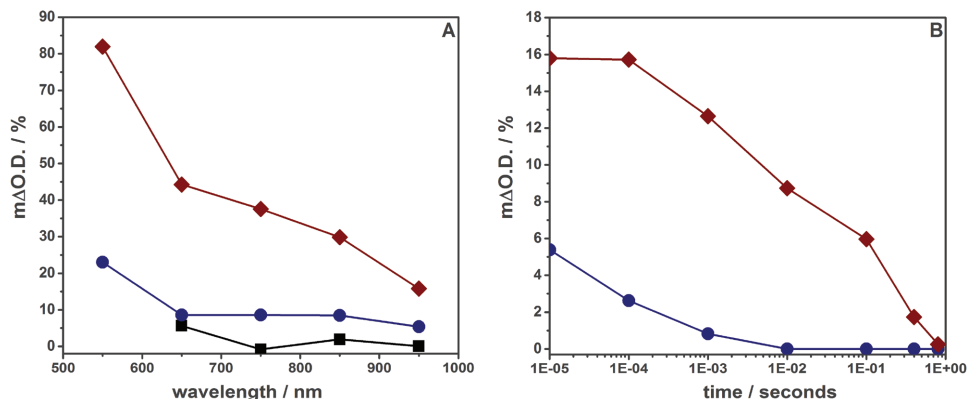


Figure 7. Transient absorption spectroscopy of the WO₃/TiO₂ heterojunction (red line) and its individual components, WO₃ (black line) and TiO₂ (blue line). A) Transient change in absorption 10 μs after a laser pulse (355 nm, 6 ns pulse width, 1.2 mJ cm^{-2} pulse⁻¹). B) Decay in transient absorption at 950 nm, which represents the recombination of photogenerated electrons located in either the WO₃ or TiO₂ layers.

Table 2. Relevant physical and functional details of the WO₃/TiO₂ film, individual analogues, and reference samples.

Sample	Physical properties			Functional properties
	Microscopy			Photocatalysis
	<i>d</i> [nm]	<i>E</i> _{bg} [eV]	Surface area [μm ²]	$\xi/10^{-4}$ [molecules photon ⁻¹]
WO ₃	–	3.10	11.1(3)	0.4 ± 0.06
TiO ₂ ^{a)}	650	3.21	4.6(4)	1.3 ± 0.04
WO ₃ /TiO ₂	100	2.85	7.6(7)	17.1 ± 0.35
WO ₃ /C/TiO ₂	100	–	7.2(7)	1.5 ± 0.07
P25 Evonik	1300	–	–	16.8 ± 0.03

^{a)}Values for a single-component TiO₂ thin film deposited on a quartz substrate under identical flow/temperature conditions and deposition time as the WO₃/TiO₂ heterojunction film. Film thickness (*d*) was of the TiO₂ layer alone and estimated using TEM, SEM, and profilometry measurements. Bandgap energy values (*E*_{bg}) were estimated from Tauc plot analysis.

a strong preferred orientation in the [002] crystal plane. The apparent inversion of the charge carrier transfer observed in our case, with electrons moving from WO₃ to TiO₂, could indeed be associated with structural differences, resulting in different electronic properties that alter the interaction between the two semiconductors. For instance, Kafizas et al.^[10] found that hole transfer in the anatase/rutile TiO₂ heterojunction flowed in a reverse direction to band model predictions determined by both computation and experiment,^[3] which was attributed to the presence of intra-bandgap defect energy levels at the heterojunction interface. Many works reported in the

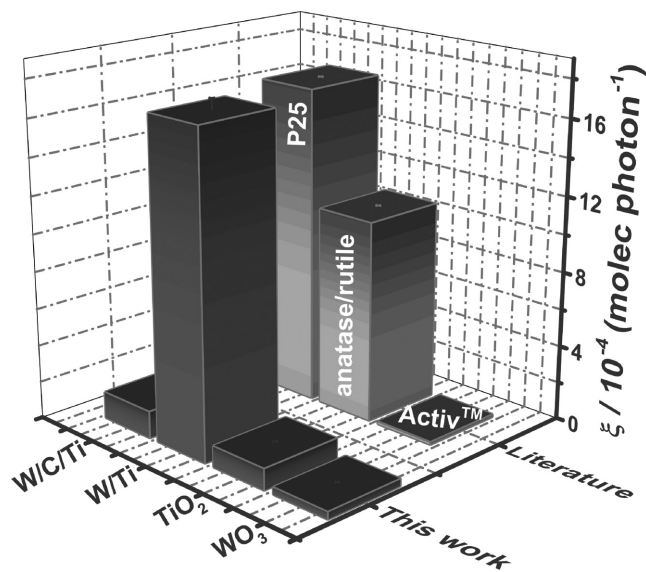


Figure 8. Photocatalytic activities of the WO₃/TiO₂ heterojunction (W/Ti), its individual analogues WO₃ and TiO₂, and a WO₃/C/TiO₂ (W/C/Ti) film, where a carbon layer was deposited between the WO₃ and TiO₂ layers. These results are expressed as formal quantum efficiencies (ξ), which represent the rate of stearic acid molecules degraded per incident photon (molecule photon⁻¹) under UVA illumination (*I* = 3.15 mW cm⁻²). Typical ξ values of relevant photocatalytic materials are included for reference. The corresponding activities of Pilkington Activ and the rutile/anatase heterojunction TiO₂ films were obtained from refs. [42] and [4].

literature use WO₃/TiO₂ composites rather than clearly defined heterojunctions.^[14,44,46] Makwana et al.^[16] developed cold-pressed WO₃/TiO₂ pellets, and found that the color of the WO₃ layer changed from yellow to blue upon radiation, resulting in the formation of reduced W^{5+/4+} species. However, our computational and HAXPES studies showed complementary evidence for a monoclinic WO₃/anatase TiO₂ band alignment that favors the transfer of photogenerated electrons into TiO₂ and holes into WO₃ (Figures 5 and 6). This direction of electron transfer is supported by the fact that no color change was observed in our WO₃/TiO₂ heterojunction films, even after long periods of intense ultraviolet illumination (i.e., several days at ≈3 mW cm⁻²).

It is worth noting that, despite the different synthetic routes and crystal structures, the WO₃/TiO₂ heterojunction system has typically shown an enhancement in function compared to the individual analogues. It is also important to establish whether the enhanced activity of the WO₃/TiO₂ film correlates with a favorable light absorption compared to its individual components. The conventional evaluation of photocatalytic activity using formal quantum efficiencies (ξ) assumes that all incident photons are effectively absorbed by the films. Ideally, the activity should be expressed in terms of quantum yield, which considers the number of absorbed photons in this evaluation. Unfortunately, this estimation is not always straightforward, particularly when using light sources of relatively broad emission spectra. As previously mentioned, the absorption spectrum of the heterojunction film showed a band onset that was substantially red-shifted compared to those of each isolated analogue. Figure 4D highlights the absorption of this film compared to a pure TiO₂ film. As indicated in the figure, it can be clearly observed that the absorption of the heterojunction film was approximately four times higher than that of the TiO₂ film at the maximum emission wavelength of the lamp ($\lambda_{\text{max}} = 365$ nm). While this is an important advantage for the WO₃/TiO₂ film, the enhancement in activity observed (14-fold with respect to TiO₂) cannot be explained solely in terms of light absorption.

The efficiency of a system in heterogeneous photocatalysis is also strongly related to the specific surface area of the catalyst. Considering the surface roughness of our WO₃/TiO₂ film, it was important to evaluate whether the enhanced photocatalytic activity of this film could be merely attributed to an increased in surface area rather than to any electronic advantage at the heterojunction level.^[5] Hence, an experiment was designed where a thin layer of carbon was sputtered over the WO₃ nanorods before the deposition of the TiO₂ layer in order to inhibit direct contact between the oxide phases. As observed by SEM (Figure S1, Supporting Information), the resulting WO₃/C/TiO₂ film had a similar microstructure to that of the WO₃/TiO₂ film. Despite the similar morphology, the WO₃/C/TiO₂ film only showed a slight increase in photocatalytic activity over the pure TiO₂ film (Figure 8) and thus the enhanced activity of the WO₃/TiO₂ film was attributed mainly to a synergistic interaction between the two semiconductors.

As previously shown, this synergistic interaction was unequivocally confirmed by our TAS studies, which showed an enhanced charge carrier population and lifetime of photogenerated charge (Figure 7). In terms of the lack of function

Table 3. Photocatalytic enhancement factors of representative heterojunction and doped materials reported in the literature. Synthetic method and photocatalytic test are included as reference. All photocatalytic materials were compared to their individual analogues.

Photocatalyst	Synthesis method	Test	λ	Enhancement factor ^{a)}	Refs.
WO ₃ /TiO ₂	(AP)CVD	Stearic acid	UVA	14	This work
Rutile/anatase TiO ₂	(AP)CVD	Stearic acid	UVA	8	4
Nano-Au:Ag:TiO ₂	Sol-gel	Stearic acid	UVA	7	50
W:TiO ₂	Sol-gel	Stearic acid	UVA	5	50
N:TiO ₂	(AP)CVD	Stearic acid	UVA	3.5	51

^{a)}Approximate enhancement factors estimated from activity ratios between the heterojunction (or chemically modified/doped) material and the corresponding active analogue (or pure) component.

observed in WO₃/C/TiO₂ our triple-junction, we attribute this to unfavorable band-bending at both semiconductor-metal interfaces, which forms an ohmic contact that encourages the flow of photogenerated electrons into the carbon layer (full details of our band modeling are provided in Figures S4 to S8, Supporting Information).

It is widely accepted that most photocatalytic processes on TiO₂, when conducted at ambient conditions, proceed via the generation of hydroxyl and superoxide radicals (from the reaction of photogenerated charges with surface-bound water and dioxygen species, respectively) that are highly active in the decomposition of organic species.^[47] The timescales in which these processes occur have been studied using TAS, being in the microsecond and millisecond timescales for the respective formation of hydroxyl radicals and superoxide species.^[48,49] Our TAS studies showed that there was a ≈ 20 -fold increase in the number of photogenerated electrons in our WO₃/TiO₂ heterojunction compared with TiO₂ from the millisecond timescale—the timescale relevant to the formation of superoxide. In addition, the rate at which these charges recombined was substantially slowed, likely reducing the competition between recombination and photogeneration. An interesting question remains as to the role of photogenerated holes in our WO₃/TiO₂ heterojunction structure. We therefore speculate that these holes either remain within the WO₃ layer or drive the formation of hydroxyl radicals at breaks in the TiO₂ coating or, more likely, also migrate into the TiO₂ layer through intrabandgap trap-states.

It is worth comparing the photocatalytic efficiency of our WO₃/TiO₂ heterojunction with the enhancements observed for different heterojunction systems and chemically modified photocatalysts. Unfortunately, a direct comparison of the photocatalytic activity with previous studies of WO₃/TiO₂ could not be conducted, as these studies were mainly based on changes in hydrophilicity.^[12,45] There is also an inherent difficulty to compare photocatalytic materials produced by different synthetic methods and research groups. This issue was bypassed herein by comparing enhancement factors of materials synthesized in our group using the same photocatalytic test, the degradation of stearic acid (Table 3). This enhancement factor was estimated from activity ratios between the heterojunction (or doped) material and their corresponding best-performing single (or pure) component. For instance, the enhancement factor for the system reported by Quesada-Cabrera et al.,^[4] rutile/anatase TiO₂ heterojunction, was calculated by taking

the ξ value for the heterojunction system and the most active single-component, anatase TiO₂, these values being ≈ 7.0 and ≈ 0.74 molecules photon⁻¹, respectively, and thus the estimated enhancement factor is ≈ 8 . As observed in Table 3, the corresponding enhancement factor of our WO₃/TiO₂ system is ≈ 14 , which is the highest enhancement ever reported, to the best of our knowledge. A more comprehensive comparison with the literature is shown in Table S1 (Supporting Information).

4. Conclusion

Nanostructured WO₃/TiO₂ heterojunction films were grown using chemical vapor deposition. To the best of our knowledge, the optimized WO₃/TiO₂ film showed the highest enhancement in photocatalytic activity compared to its single-semiconductor analogues. The WO₃/TiO₂ heterojunctions showed an unusual electron transfer from WO₃ to TiO₂. A direct understanding of this charge transfer process was provided through both computational calculation and experiment (HAXPES and TAS).

Importantly, the WO₃/TiO₂ films are durable and the results observed are highly reproducible over multiple photocatalytic cycles. The methods described here represent a breakthrough in the development of photocatalytic surfaces and highlight the advantage of using a combination of key experimental and computational techniques to develop our understanding of photocatalytic heterojunction materials, and should serve as guide to future advances in the field.

5. Experimental Section

Synthesis of the WO₃/TiO₂ Heterojunction Films: Details of the synthesis of the WO₃/TiO₂ heterojunction films as well as reference materials, WO₃/C/TiO₂ and P25 Evonik films, are given in the Supporting Information. Briefly, the WO₃/TiO₂ films were produced following a two-step process using two CVD methods. The WO₃ nanorods were deposited using aerosol-assisted CVD from a 2:1 mixture of acetone (99%) and methanol (99.5%) dispersion (15 mL) of tungsten hexacarbonyl (W(CO)₆, 0.060 g, 99%). The solution containing the precursors was moistened using an ultrasonic humidifier (Liquifog, Johnson Matthey) operating at 2 MHz. Pure tungsten trioxide (WO₃) nanorods were deposited as a thin film at a set temperature of 375 °C (the actual temperature ranged between 339 and 358 °C) on quartz slides (Multi-Lab). In the optimum WO₃/TiO₂ heterojunction film discussed here the WO₃ nanorods were $\approx 650 \times 60$ nm (length \times width). After the synthesis of the WO₃ nanorods, an anatase TiO₂ overlayer

was deposited at 500 °C from titanium tetrachloride (TiCl₄, 99%) and ethyl acetate (C₄H₈O₂, 99.8%) using atmospheric-pressure CVD. Each precursor was heated in stainless steel bubblers at 70 and 40 °C, respectively, and their flow rates set at 1.2 and 0.25 L min⁻¹, respectively. The precursors were mixed in a stainless steel chamber (250 °C) before accessing the reactor. In the optimum film, the WO₃ nanorods were conformally coated with a TiO₂ overlayer of ≈100 nm thickness.

Physical Characterization: XRD analysis was performed using a Bruker-Axs D8 (Lynxeye XE) diffractometer. The instrument operates with a Cu X-ray source, monochromated (Kα₁, 1.54 Å). The films were analyzed with a glancing incident angle (θ) of 1°. Le Bail fits were carried out using structure parameters from Joint Committee on Powder Diffraction Standards, using GSAS and EXPGUI software suit. Raman spectroscopy was carried out using a Renishaw 1000 spectrometer equipped with a 633 nm laser. The Raman system was calibrated using a silicon reference. UV-vis spectroscopy was performed using a Perkin Elmer Lambda 950 UV/vis/NIR Spectrophotometer in the 300–2500 nm range. A *Labsphere* reflectance standard was used as reference in the UV-vis measurements. SEM studies were carried out using a JEOL 6301 (5 KV) and a JEOL JSM-6700F field emission instruments. HRTEM images were obtained using a high-resolution TEM JEOL 2100 with a LaB₆ source operating at an acceleration voltage of 200 kV. Images were recorded on a Gatan Orius charge-coupled device. The films were scrapped off the quartz substrate using a diamond pen, sonicated and suspended in methanol and drop-casted onto a 400 Cu mesh lacy carbon film grid (Agar Scientific Ltd.) for TEM analysis. EDS analysis was carried out using a JEOL JSM-6700F and secondary electron image on a Hitachi S-3400N field emission instruments (20 KV) and the Oxford software INCA. Atomic force microscopy was conducted using a Bruker Icon system running in PeakForce quantitative nanomechanical property mapping) mode. Bruker NCHV (etched silicon) tips were used in contact mode over a selection of 5 μm × 5 μm areas to measure the topography of the samples. XPS was performed using a Thermo K alpha spectrometer with monochromated Al K alpha radiation, a dual beam charge compensation system and constant pass energy of 50 eV. Survey scans were collected in the range of 0–1200 eV. High resolution peaks were used for the principal peaks of Ti (2p), W (4f), O (2p), and C (1s). The peaks were modeled using sensitivity factors to calculate the film composition. The area underneath these bands was an indication of the element concentration within the region of analysis (spot size 400 μm).

Theoretical Characterization: All calculations were performed using the VASP code,^[52–55] a periodic plane wave DFT code where the interactions between the core and valence electrons were dealt with using the project augmented wave method.^[56] Both the plane wave basis set and k-point sampling were checked for convergence, with a cutoff of 560 eV and k-point grid of Γ -centered 4 × 4 × 4, for the 32 atom monoclinic unit cell of WO₃ found to be sufficient. Geometry optimizations were performed using the HSE06 hybrid DFT functional.^[25] The structures were deemed to be converged when the forces on all the atoms totaled less than 10 meV Å⁻¹. In the plane wave formalism, due to the presence of periodic boundary conditions, the electrostatic potential of a crystal was not defined with respect to an external vacuum level and, as such, the absolute electronic eigenvalues from different calculations were not comparable. In order to align the energies to the vacuum level, a slab-gap model (128 atom, 15.5 Å slab, 20 Å vacuum) was constructed and the corresponding electrostatic potential averaged along the *c*-direction, using the MacroDensity package.^[24] Consistent with previous studies of WO₃ surfaces,^[57] a (√2 × √2)R45° reconstruction of the (001) surface was cleaved using the METADISE code.^[58]

Transient Absorption Spectroscopy: Transient absorption spectroscopy, from the microsecond to second timescale, was measured in diffuse reflectance mode. The experimental setup used an Nd:YAG laser (OPOTEK Opolette 355 II, 7 ns pulse width) as the excitation source. 355 nm light was generated from the third harmonic of the laser and transmitted to the sample through a light guide to photoexcite the thin film samples. An excitation power density of 1.2 mJ cm⁻² and laser repetition rates of 0.9 Hz was used. As the changes of reflectance observed were low (<1%), it was assumed that the transient signal was

directly proportional to the concentration of excited state species. The probe light source was a 100 W Bentham IL1 quartz halogen lamp. Long pass filters (Comar Instruments) between the lamp and sample were used to minimize short wavelength irradiation of the sample. Diffuse reflectance from the sample was collected by a 2" diameter, 2" focal length lens and relayed to a monochromator (Oriol Cornerstone 130) to select the probe wavelength. Time-resolved intensity data were collected with an Si photodiode (Hamamatsu S3071). Data at times faster than 3.6 ms were recorded by an oscilloscope (Tektronics DPO3012) after passing through an amplifier box (Costronics) while data slower than 3.6 ms were simultaneously recorded on a National Instrument DAQ card (NI USB-6251). Each kinetic trace was obtained from the average of 100–200 laser pulses. Acquisitions were triggered by a photodiode (Thorlabs DET10A) exposed to laser scatter. Data were acquired and processed using home-built software written in the Labview environment.

Photocatalytic Tests: Details of the photocatalytic tests are given in the Supporting Information. A Perkin Elmer RX-I Fourier transform infrared spectrometer was used to monitor the degradation of stearic acid on the films under UVA irradiation. In a typical test, a thin layer of stearic was deposited onto the film using a home-made dip-coater from a 0.05 M stearic acid solution on chloroform. The number of acid molecules degraded was estimated using the conversion factor 1 cm⁻¹ ≡ 9.7 × 10¹⁵ molecule cm⁻² from the literature.^[39] The photoactivity rates were estimated from linear regression of the initial 30%–40% steps (zero-order kinetics) of the area curves. The results were typically expressed in terms of the formal quantum efficiency, ξ, defined as the number of molecules degraded per incident photon (units, molecules photon⁻¹). The light source was a blacklight-bulb lamp, 2 × 8 W (Vilber-Lourmat). The irradiance of the lamp (*I* = 3.15 mW cm⁻²) was measured using a UVX radiometer (UVP).

Supporting Information

Supporting Information is available from the Wiley Online Library or from the author.

Acknowledgements

C.S.-V. and R.Q.-C. were supported by the European Seventh Framework Programme (PCATDES Project, No. 309846). This work made use of the ARCHER UK National Supercomputing Service (<http://www.archer.ac.uk>), via the membership of the UK's HEC Materials Chemistry Consortium, which was funded by EPSRC (EP/L000202). A.K. thanks the Ramsay Memorial Fellowships Trust for funding. Dr. Sanjay Sathasivam and Dr. Francesco Di Maggio are thanked for useful discussion. Dr. Steven Firth and Mr. Martin Vickers are also thanked for access to SEM, TEM, Raman, and XRD instruments.

[1] M. Gratzel, *J. Photochem. Photobiol.*, **C** **2003**, *4*, 145.

[2] S. J. A. Moniz, S. A. Shevlin, D. J. Martin, Z.-X. Guo, J. Tang, *Energy Environ. Sci.* **2015**, *8*, 715.

[3] D. O. Scanlon, C. W. Dunnill, J. Buckeridge, S. A. Shevlin, A. J. Logsdail, S. M. Woodley, C. R. A. Catlow, M. J. Powell, R. G. Palgrave, I. P. Parkin, G. W. Watson, T. W. Keal, P. Sherwood, A. Walsh, A. A. Sokol, *Nat. Mater.* **2013**, *12*, 798.

[4] R. Quesada-Cabrera, C. Sotelo-Vazquez, J. C. Bear, J. A. Darr, I. P. Parkin, *Adv. Mater. Interfaces* **2014**, *1*, 1400069.

[5] H. Wang, L. Zhang, Z. Chen, J. Hu, S. Li, *Chem. Soc. Rev.* **2014**, *43*, 5234.

- [6] B. Ohtani, O. O. Prieto-Mahaney, D. Li, R. Abe, *J. Photochem. Photobiol., A* **2010**, 216, 179.
- [7] A. Paracchino, V. Laporte, K. Sivula, M. Gratzel, E. Thimsen, *Nat. Mater.* **2011**, 10, 456.
- [8] J. Su, L. Guo, N. Bao, C. A. Grimes, *Nano Lett.* **2011**, 11, 1928.
- [9] S. J. A. Moniz, J. Zhu, J. Tang, *Adv. Energy Mater.* **2014**, 4, 1301590.
- [10] A. Kafizas, X. Wang, S. R. Pendlebury, P. Barnes, M. Ling, C. Sotelo-Vazquez, R. Quesada-Cabrera, C. Li, I. P. Parkin, J. R. Durrant, *J. Phys. Chem. A* **2016**, 120, 715.
- [11] D. C. Hurum, A. G. Agrios, K. A. Gray, T. Rajh, M. C. Thurnauer, *J. Phys. Chem. B* **2003**, 107, 4545.
- [12] M. Miyauchi, A. Nakajima, T. Watanabe, K. Hashimoto, *Chem. Mater.* **2002**, 14, 4714.
- [13] W. Smith, A. Wolcott, R. C. Fitzmorris, J. Z. Zhang, Y. Zhao, *J. Mater. Chem.* **2011**, 21, 10792.
- [14] S. Higashimoto, M. Sakiyama, M. Azuma, *Thin Solid Films* **2006**, 503, 201.
- [15] G. Leftheriotis, S. Papaefthimiou, P. Yianoulis, A. Siokou, *Thin Solid Films* **2001**, 384, 298.
- [16] N. M. Makwana, R. Quesada-cabrera, I. P. Parkin, P. F. Mcmillan, A. Mills, J. A. Darr, *J. Mater. Chem. A* **2014**, 2, 17602.
- [17] M. Ling, C. Blackman, *Phys. Status Solidi C* **2015**, 12, 869.
- [18] A. Kafizas, I. P. Parkin, *J. Am. Chem. Soc.* **2011**, 133, 20458.
- [19] M. Ling, C. Blackman, R. Palgrave, C. Sotelo-Vazquez, A. Kafizas, Ivan P. Parkin, *Adv. Mater. Interfaces* **2017**, admi.201700064.
- [20] A. M. Smith, M. G. Kast, B. A. Nail, S. Aloni, S. W. Boettcher, *J. Mater. Chem. A* **2014**, 2, 6121.
- [21] J. Tauc, *Mater. Res. Bull.* **1968**, 3, 37.
- [22] Y. Hinuma, A. Gruneis, G. Kresse, F. Oba, *Phys. Rev. B* **2014**, 90, 155405.
- [23] J. Buckeridge, K. T. Butler, C. R. A. Catlow, A. J. Logsdail, D. O. Scanlon, S. A. Shevlin, S. M. Woodley, A. A. Sokol, A. Walsh, *Chem. Mater.* **2015**, 27, 132111.
- [24] L. A. Burton, A. Walsh, *Appl. Phys. Lett.* **2016**, 120, 132111.
- [25] A. V. Krukau, A. O. Vydrov, A. F. Izmaylov, G. E. Scuseria, *J. Chem. Phys.* **2007**, 1225, 224106.
- [26] L. Weinhardt, M. Blum, M. Bar, C. Heske, B. Cole, B. Marsen, E. L. Miller, *J. Phys. Chem. C* **2008**, 112, 3078.
- [27] R. L. Anderson, *IBM J. Res. Dev.* **1960**, 4, 283.
- [28] S. R. Pendlebury, X. Wang, F. Formal, M. Le Cornuz, A. Kafizas, S. D. Tilley, M. Gra, J. R. Durrant, *J. Am. Chem. Soc.* **2014**, 136, 9854.
- [29] F. M. Pesci, A. J. Cowan, B. D. Alexander, J. R. Durrant, D. R. Klug, *J. Phys. Chem. Lett.* **2011**, 2, 1900.
- [30] Y. Ma, S. R. Pendlebury, A. Reynal, F. L. Formal, R. J. Durrant, *Chem. Sci.* **2014**, 5, 2964.
- [31] A. Fujishima, X. Zhang, D. Tryk, *Surf. Sci. Rep.* **2008**, 63, 515.
- [32] L. Wang, C. McCleese, A. Kovalsky, Y. Zhao, C. Burda, *J. Am. Chem. Soc.* **2014**, 136, 12205.
- [33] T. M. Clarke, F. C. Jamieson, J. R. Durrant, *J. Phys. Chem. C* **2009**, 113, 20934.
- [34] L. Wang, H.-Y. Wang, B.-R. Gao, L.-Y. Pan, Y. Jiang, Q.-D. Chen, W. Han, H.-B. Sun, *IEEE J. Quantum Electron.* **2011**, 47, 1177.
- [35] S. Devahasdin, C. Fan, K. Li, D. H. Chen, *J. Photochem. Photobiol., A* **2003**, 156, 161.
- [36] J. Tang, J. R. Durrant, D. R. Klug, *J. Am. Chem. Soc.* **2008**, 130, 13885.
- [37] X. Wang, A. Ka, X. Li, S. J. A. Moniz, P. J. T. Reardon, J. Tang, I. P. Parkin, J. R. Durrant, *J. Phys. Chem. C* **2015**, 119, 10439.
- [38] A. J. Cowan, W. Leng, P. R. F. Barnes, D. R. Klug, J. R. Durrant, *Phys. Chem. Chem. Phys.* **2013**, 15, 8772.
- [39] A. Mills, J. Wang, *J. Photochem. Photobiol., A* **2006**, 182, 181.
- [40] A. Mills, M. McFarlane, *Catal. Today* **2007**, 129, 22.
- [41] A. Mills, J. Wang, *J. Photochem. Photobiol., A* **1998**, 118, 53.
- [42] A. Mills, A. Lepre, N. Elliott, S. Bhopal, I. P. Parkin, S. A. O. Neill, *J. Photochem. Photobiol., A* **2003**, 160, 213.
- [43] B. Lu, X. Li, T. Wang, E. Xie, Z. Xu, *J. Mater. Chem. A* **2013**, 1, 3900.
- [44] R. Quesada-Cabrera, E. R. Latimer, A. Kafizas, C. S. Blackman, C. J. Carmalt, I. P. Parkin, *J. Photochem. Photobiol., A* **2012**, 239, 60.
- [45] H. Irie, H. Mori, K. Hashimoto, *Vacuum* **2004**, 74, 625.
- [46] V. Puddu, R. Mokaya, G. Li Puma, *Chem. Commun.* **2007**, 45, 4749.
- [47] A. Mills, S. Le Hunte, *J. Photochem. Photobiol., A* **1997**, 108, 1.
- [48] A. Yamakata, T. Ishibashi, H. Onishi, *J. Phys. Chem. B* **2001**, 105, 7258.
- [49] L. Xiao-e, A. N. M. Green, S. A. Haque, A. Mills, J. R. Durrant, *J. Photochem. Photobiol., A* **2004**, 162, 253.
- [50] A. Kafizas, S. Kellici, J. A. Darr, I. P. Parkin, *J. Photochem. Photobiol., A* **2009**, 204, 183.
- [51] C. Sotelo-Vazquez, R. Quesada-Cabrera, J. A. Darr, I. P. Parkin, *J. Mater. Chem. A* **2014**, 2, 7082.
- [52] G. Kresse, J. Hafner, *Phys. Rev. B* **1993**, 47, 558.
- [53] G. Kresse, J. Hafner, *Phys. Rev. B* **1994**, 49, 14251.
- [54] G. Kresse, J. Furthmuller, *Phys. Rev. B* **1996**, 54, 11169.
- [55] G. Kresse, J. Furthmuller, *Comput. Mater. Sci.* **1996**, 6, 15.
- [56] G. Kresse, D. Joubert, *Phys. Rev. B* **1999**, 59, 11.
- [57] P. M. Oliver, S. C. Parker, R. G. Egdell, F. H. Jones, *J. Chem. Soc., Faraday Trans.* **1996**, 92, 2049.
- [58] G. W. Watson, E. T. Kelsey, N. H. De Leeuw, D. J. Harris, S. C. Parker, *J. Chem. Soc., Faraday Trans.* **1996**, 92, 433.